MOLECULAR SIMULATION, 2016
VOL. 42, NO. 13, 1102–1115
http://dx.doi.org/10.1080/08927022.2015.1123257

Taylor & Francis
Taylor & Francis Group

Models for recovering the energy landscape of conformational transitions from single-molecule pulling experiments

Gaurav Arya

Department of NanoEngineering, University of California, San Diego, La Jolla, CA, USA

ABSTRACT

Single-molecule force spectroscopy is a powerful experimental technique for probing intermolecular forces and conformational transitions of individual molecules. This technique involves measuring the mechanical response of a molecule subjected to a constant or time-varying force. Statistical mechanics has played a pivotal role in interpreting force measurements in terms of the underlying kinetics and energy landscape of the molecular transition being studied. Here, we provide a didactic review of various statistical–mechanical models used for analysing these measurements, emphasising the theoretical ideas and assumptions used in deriving these models.

ARTICLE HISTORY
Received 14 September 2015
Accepted 14 November 2015

KEYWORDS
Force spectroscopy; rupture force; force ramp; optical trap; AFM pulling; Bell model

Gaurav Arya is currently Associate Professor in the Department of NanoEngineering at the University of California, San Diego (UCSD). He received his BTech in Chemical Engineering from the Indian Institute of Technology, Bombay in 1998, and PhD, in Chemical Engineering, from the University of Notre Dame in 2003 studying diffusion of gases through nanoporous materials. He did his postdoctoral research at Princeton University and held an assistant research scientist position at New York University prior to joining UCSD as an assistant professor. His research group develops and uses advanced molecular simulation techniques to study a variety of biomolecular and nanoengineering systems of interest, including genome organisation and regulation, viral DNA packaging motors, DNA-based nanomachines and polymer-nanoparticle composites.

1. Introduction

How molecules fold or unfold, bind to each other and undergo internal conformational changes is fundamentally related to the underlying energy landscape, defined as the potential energy $U(\mathbf{r}^N)$ of the molecular system as a function of all its possible conformations specified by the Cartesian coordinates $\mathbf{r}^N \equiv \{x_1, y_1, z_1, x_2, y_2, z_2, \cdots, x_N, y_N, z_N\}$ for an N-atom system.[1] Consider a conformational transition from one stable state, identified by a minimum in the energy landscape and denoted by **R** (as in 'reactant') to another stable state denoted by **P** (as in 'product') in the landscape (Figure 1(A)). Given the stochastic nature of molecular transitions due to thermal fluctuations, the transition may be pictured [2] as an ensemble of 'productive' trajectories traversing across this multi-dimensional landscape, each originating from **R** and ending at **P**, with most of the trajectories passing through a transition state, identified as the saddle point in the landscape and denoted by **T**.

In many cases, the transition can be approximated as a combination of deterministic and stochastic motion along a single coordinate x known as the 'reaction coordinate' connecting the two stable states via the transition state (Figure 1(A) and (B)). The relevant potential along this reaction path is the free energy, or more specifically, the potential of mean force $G(x)$ defined as [3]

$$G(x) = -k_B T \ln \left\{ \int \cdots \int \delta\left(x'(\mathbf{r}^N) - x\right) \exp\left[-U(\mathbf{r}^N)/k_B T\right] d\mathbf{r}^N \right\} \quad (1)$$

to within an additive constant, where x specifies the position along the reaction coordinate and $x'(\mathbf{r}^N)$ is a function describing the reaction coordinate in terms of the relevant degrees of freedom. The resulting 1D free-energy landscape allows characterization of the molecular transition in terms of three parameters (Figure 1(B)): (1) the distance Δx_0 of the energy barrier at the transition state from the reactant state, (2) the height ΔG_0 of this energy barrier relative to the reactant state and (3) the intrinsic rate k_0 of transition across the barrier, from reactant to product. Because the Boltzmann factor $\exp\left[-U/k_B T\right]$ in Equation (1) is integrated over all degrees of freedom $\mathbf{r}^N$, $G(x)$ naturally accounts for energetic and entropic variations along x. Therefore, if the saddle region in Figure 1(A) were much narrower than the two minima, a portion of ΔG_0 shown in Figure 1(B) would also arise from the low entropy of the transition state, in addition to its high energy.

A powerful approach for experimentally probing the energy landscape of molecular transitions is single-molecule force spectroscopy (SMFS).[4] This approach, developed in the 1990s, involves studying the mechanical response of individual molecules

CONTACT Gaurav Arya garya@ucsd.edu
This article was originally published with errors. This version has been corrected/amended. Please see Erratum (http://dx.doi.org/10.1080/08927022.2016.1259874).

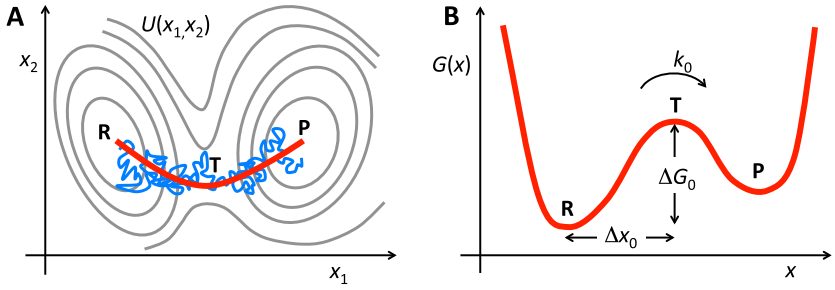

Figure 1. (A) Molecular transition between two stable states across a transition state in a multi-dimensional energy landscape, illustrated using the example of a contour plot of a 2D potential energy landscape $U(x_1, x_2)$ with two independent coordinates x_1 and x_2. A hypothetical molecular trajectory $(x_1(t), x_2(t))$ is shown in blue and a possible reaction coordinate is shown in red. (B) Schematic of 1D free-energy landscape obtained from a projection of the 2D potential energy landscape onto the reaction coordinate showing parameters k_0, Δx_0 and ΔG_0 that characterise the molecular transition.

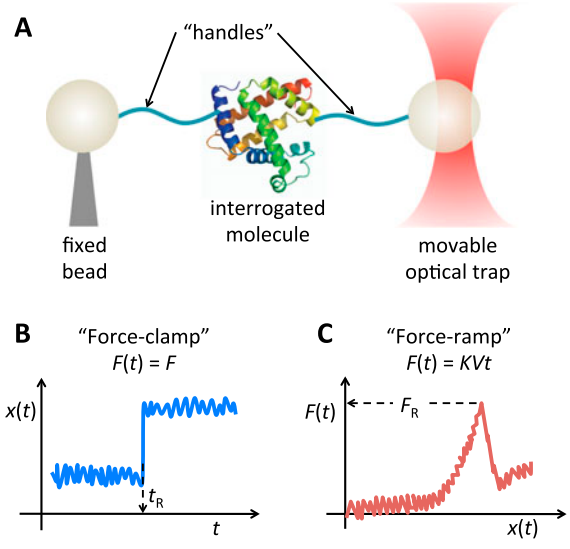

Figure 2. (A) Schematic showing a typical optical tweezers SMFS set-up for imposing a time-varying force $F(t)$ on the interrogated molecule via a movable optical trap (figure not to scale). Schematic of the typical outputs obtained in the (B) constant-force and (C) constant-speed pulling modes.

subjected to controlled forces through a pulling device (Figure 2(A)). The most common pulling devices include the atomic force microscope (AFM), optical tweezers (OT) and magnetic tweezers (MT).[5] The underlying principle behind each technique is the same: one end of the molecule or the molecular complex is attached to a fixed support while the other end is attached to a probe – the tip of the cantilever beam in AFM, the dielectric bead in OT and the magnetic bead in MT – through which the force is imposed, and measured. The force is imposed by translating the mechanical element or electromagnetic field coupled to the probe – the end of the cantilever beam in AFM, the laser optical trap in OT and the magnetic field in MT – causing a deflection δx in the probe from its equilibrium position. Assuming Hookean spring behaviour of the probe, the imposed force is then obtained via $F = -K\delta x$, where K is the effective spring constant of the probe. Thus, by manipulating the coupling agent in a time-dependent manner, a time-varying pulling force $F(t)$ may be imposed on the attached molecule.

SMFS experiments are operated most commonly in two pulling modes.[4] In the 'force-clamp' mode, a constant pulling force F is imposed and the molecular extension (end-to-end distance) $x(t)$ is monitored as a function of time t. A sudden jump in the extension signals a rupture event, with the corresponding time termed 'rupture time' t_R (Figure 2(B)). By 'rupture', we mean sudden unfolding of a molecule or dissociation of a molecular complex through breakage of the intermolecular bonds holding together the molecule or complex. Repeated measurements at the same force should yield an average time constant of rupture, which can be inverted to obtain the average rate constant $k(F)$ of rupture that is expected to increase rapidly with the magnitude of the applied force. An even more popular pulling mode is the 'force-ramp' mode, where the pulling device is pulled at a constant speed V, resulting in a linearly increasing applied force approximately given by $F(t) = KVt$, where $\dot{F} \equiv KV$ is the so-called loading rate. Rupture is detected as a 'rip' in the force-extension (F-x) plot (Figure 2(C)) and the associated force is termed the 'rupture force' F_R. Repeated measurements yield a loading rate-dependent distribution $p(F_R; \dot{F})$ in rupture forces, which can then be averaged to obtain the mean rupture force $\overline{F_R}(\dot{F})$. Two other pulling modes, the constant-position and force-jump protocols, [4] which are less commonly employed will not be discussed here.

Statistical mechanics has played a critical role in making sense of such rate and force measurements emerging from SMFS experiments, specifically in recovering properties of the underlying free-energy landscape. In this review, we provide a historical account of some of the key statistical–mechanical models developed over the years to extract these parameters from rupture rate and force measurements. In particular, we focus on a class of analytical models that relate rupture rates, forces and distributions to the height ΔG_0 of the energy barrier, its location Δx_0, and the intrinsic rate constant k_0 associated with the free-energy landscape governing the rupture transition. A different class of models [6,7] based on Jarzynski's equality [8] and Crooks' fluctuation theorem [9] involving work measurements for recovering properties of the energy landscape are not discussed. We begin by discussing the earlier models, termed first-generation models, based on the Bell–Zhurkov phenomenological force-rate relationship. Next, we discuss more sophisticated models, second-generation models, based on Kramers' theory and functional forms of the energy landscape. Lastly, we discuss more recent models, third-generation models, accounting for the stiffness of the pulling device and handles. We end this review by discussing the role of molecular simulations in the development and validation of such models. Throughout this review, the focus is more on educating the readers on the theoretical concepts and assumptions

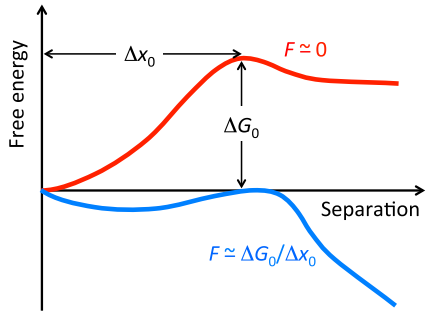

Figure 3. Schematic of the free energy of separation of two bound molecules as a function of their separation distance (adapted from Figure 6 of Bell [10]). The application of force decreases the free energy linearly with distance.

underpinning these models and less on their implementation and applications.

2. First-generation models

2.1. Bell–Zhurkov phenomenological model

One of the earliest models used in SMFS is the phenomenological model proposed by Bell in 1978 to describe the effect of an external force on the lifetime of a receptor–ligand bond at the interface of two cells.[10] Bell surmised that the free energy of the bound molecules must exhibit a minimum at their equilibrium binding location and a maximum (barrier) between the bound and unbound states, and that work must be done to separate the molecules (Figure 3). Therefore, when a force was applied to separate the molecules, the energy barrier would diminish and, for a sufficiently strong force, completely disappear. It was further asserted that if ΔG_0 is the height of the energy barrier and Δx_0 is the distance of the minimum to the energy barrier, then the energy barrier would completely vanish at an applied force of $F_0 \simeq \Delta G_0/\Delta x_0$, as shown in Figure 3, at which point the work done $F_0 \times \Delta x_0$ equals the barrier energy ΔG_0.

To quantify the lifetime τ of the bond as a function of force F, Bell considered a relationship from Zhurkov [11] describing the lifetime of solid specimens subjected to tensile stresses:

$$\tau = \tau_0 \exp\left[\frac{(E_0 - \gamma F)}{k_B T}\right], \tag{2}$$

where τ_0 denoted the reciprocal of a natural frequency of oscillation of atoms in solids, E_0 was interpreted as an energy barrier determining the probability of bond breakage, γ was an empirical parameter introduced to quantify the strength of solids, k_B is the Boltzmann constant, and T the temperature. By setting $E_0 = \Delta G_0$, and $\gamma \simeq \Delta x_0$ so that $\tau = \tau_0$ when $F = \Delta G_0/\Delta x_0$, Bell proposed the following force-dependent unbinding rate constant $k(F)$ for a receptor–ligand bond:

$$k(F) = k_0 \exp\left(\frac{F\Delta x_0}{k_B T}\right), \tag{3}$$

where $k_0 \equiv \tau_0^{-1} \exp(-\Delta G_0/k_B T)$ is the intrinsic unbinding rate (at zero loads).

The above model for $k(F)$ has been widely used to treat the kinetics of a variety of molecular systems subjected to constant forces. In particular, the model has been fitted to rupture rate $k(F)$ measurements carried out in the force-clamp mode for recovering the intrinsic transition rate k_0 as well as distance to the activation barrier Δx_0.[12,13] However, as we will discuss later, the Bell–Zhurkov model has a number of limitations, including its inability to relate rupture rates to the energy barrier ΔG_0. Such limitations have been addressed by more sophisticated models.

2.2. Survival-probability formalism for obtaining rupture forces

As mentioned earlier, a more useful pulling mode is force-ramp, in which the pulling device of effective stiffness K is moved at a constant speed V, imposing a linearly increasing load $F(t) = KVt$ on the molecule at a constant loading rate of $\dot{F} \equiv \mathrm{d}F/\mathrm{d}t = KV$. Such a scenario was considered in 1991 by Evans and co-workers [14] in the context of agglutinin-bonded red blood cells. Specifically, the authors were attempting to measure the strength of a focal bond between two smooth membrane capsules by withdrawing one capsule from the other and recording the force F_R at the time the bond ruptured. Instead of observing a discrete rupture force each time the measurement was carried out at the same withdrawal rate, the authors observed a distribution $p(F_R)$ of rupture forces. It was rationalised that bond rupture might be a stochastic event, where the probability of survival of a bond decreases with both the duration of the load and its magnitude. It was only several years later that Evans and Ritchie [15] proposed a quantitative model for this phenomenon.

The model invokes the concept of survival probability $S(t)$, defined as the probability that the bond has *not* ruptured by time t.[15,16] Assuming that bonds do not reform once ruptured, the rate of change of survival probability is assumed to follow the first-order rate equation:

$$\frac{\mathrm{d}S(t)}{\mathrm{d}t} = -k(F(t))S(t), \tag{4}$$

where the rupture rate $k(F)$ is an indirect function of time through the time-dependency of the applied force $F(t)$. The above equation implies that the probability that a bond will rupture between time t and $t + \mathrm{d}t$ is equal to the conditional probability $k(t)\mathrm{d}t$ of an intact bond rupturing multiplied by the probability $S(t)$ that the bond has not ruptured earlier during time interval from 0 to t. Integrating the above equation within the limits $S = 1$ at time $t' = 0$ and $S = S(t)$ at time $t' = t$ then yields

$$S(t) = \exp\left[-\int_0^t k(t')\mathrm{d}t'\right]. \tag{5}$$

Substituting the Bell–Zhurkov rate constant (Equation (3)) and the force variation $F = \dot{F}t$ into Equation (5) yields the following analytical expression for $S(t)$:

$$S(t) = \exp\left[\frac{k_0 k_B T}{\dot{F}\Delta x_0}\left\{1 - \exp\left(\frac{\dot{F}\Delta x_0}{k_B T}t\right)\right\}\right], \tag{6}$$

which rightfully drops from a value of 1 at time $t = 0$ to 0 as $t \to \infty$ (see Figure 4(A)).

The survival probability $S(t)$ can be related to the distribution $p(F_R)$ of rupture forces measured from multiple pulling

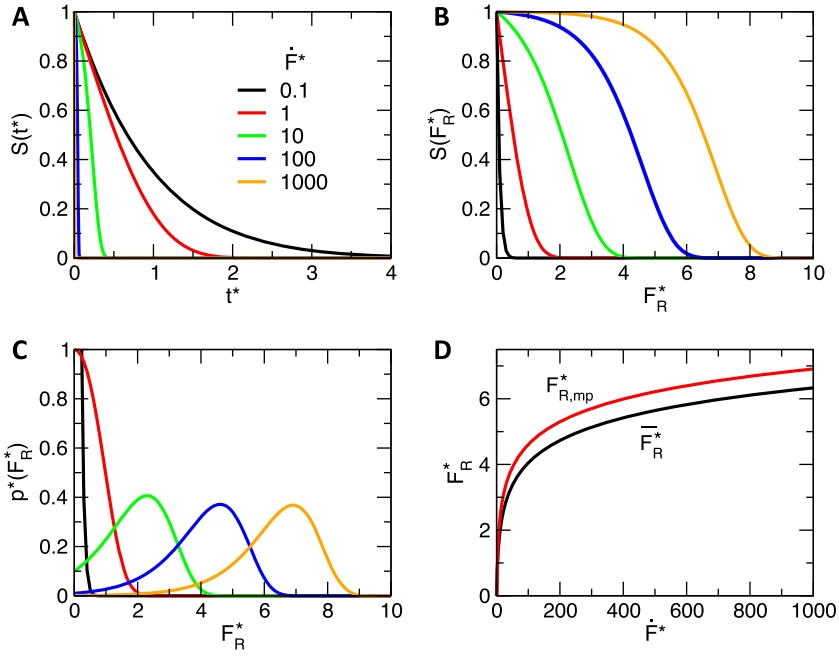

Figure 4. Characteristics of rupture under a linearly increasing force. (A) Survival probability $S(t^*)$ versus time for five different loading rates $\dot{F}^*$. (B) Survival probability $S(F_R^*)$ versus rupture force F_R^* for the five loading rates specified above. (C) Rupture force distributions $p^*(F_R^*)$ for the same five loading rates. (D) Mean rupture force $\overline{F_R}^*$ and most-probable force $F_{R,mp}^*$ plotted as a function of loading rate. All quantities are plotted in dimensionless units: $t^* \equiv k_0 t$, $\dot{F}^* \equiv \dot{F}\Delta x_0/k_0 k_B T$, $F_R^* \equiv F_R \Delta x_0/k_B T$, $p^*(F_R^*) \equiv k_B T p(F_R^*)/\Delta x_0$, $\overline{F_R}^* \equiv \overline{F_R}\Delta x_0/k_B T$, and $F_{R,mp}^* \equiv F_{R,mp}\Delta x_0/k_B T$.

experiments at the same loading rate $\dot{F}$ given that the measured F_R can be related to the pulling time t via $F_R = \dot{F}t$, i.e. $S(t) \equiv S(t(F_R))$. By definition, the fraction of bonds that have ruptured on average by the time t the load has risen to a value of F_R is given by $\int_0^{F_R} p(F'_R)\mathrm{d}F'_R$. Note how this fraction is 0 at the start of pulling ($t = 0$) when $F_R = 0$ and equals 1 after pulling for an infinite time whereupon $F_R \to \infty$. This ruptured fraction is also by definition equal to 1 minus the probability $S(t)$ that a bond has survived by time t. In other words, $1 - S(t) = \int_0^{F_R} p(F'_R)\mathrm{d}F'_R$. Differentiating both sides with respect to F_R yields

$$-\mathrm{d}S = p(F_R)\mathrm{d}F_R. \tag{7}$$

Differentiating further both sides with respect to time, recognising that $\mathrm{d}F_R/\mathrm{d}t = \dot{F}$, and substituting Equation (4) yields

$$p(F_R) = \frac{1}{\dot{F}} k(F_R) S(t). \tag{8}$$

Substituting Equation (5) into the above equation and changing the variable of integration from t to F_R yields the following explicit formula for obtaining $p(F_R)$:

$$p(F_R) = \frac{k(F_R)}{\dot{F}} \exp\left[-\int_0^{F_R} \frac{k(F)}{\dot{F}}\mathrm{d}F\right]. \tag{9}$$

An explicit expression for $p(F_R)$ corresponding to the Bell–Zhurkov model may be obtained by substituting Equation (3) into Equation (9):

$$p(F_R) = \frac{k_0}{\dot{F}} \exp\left[\frac{F_R \Delta x_0}{k_B T}\right] \exp\left[\frac{k_0 k_B T}{\dot{F}\Delta x_0}\left\{1 - \exp\left[\frac{F_R \Delta x_0}{k_B T}\right]\right\}\right]. \tag{10}$$

The resulting $p(F_R)$, plotted in Figure 4(C), correctly predicts the characteristic bell-like shape of rupture force histograms observed experimentally at intermediate to large loading rates. Equation (8) provides a simple mathematical explanation for this shape: $k(F_R)$ is a rapidly increasing function of force (from Equation (3)) while $S(t)$ is a rapidly decreasing function of time (or force) (Figure 4(A)), causing their product $k(F_R)S(t) \sim p(F_R)$ to exhibit a maximum at an intermediate force. A more intuitive explanation is that at small forces, the bond does not get enough time to rupture, leading to a small rupture probability $p(F_R)$, whereas at large forces, only a few intact bonds remain as most molecules have already ruptured at lower forces, also leading to a small $p(F_R)$. The largest value of $p(F_R)$ is then expected to occur at some intermediate force. It can further be shown that in the limit of low forces, $p(F_R)$ rises exponentially with F_R as

$$\lim_{F_R \to 0} p(F_R) \approx \frac{k_0}{\dot{F}} \exp\left[\frac{F_R \Delta x_0}{k_B T}\left(1 - \frac{k_0 k_B T}{\dot{F}\Delta x_0}\right)\right], \tag{11}$$

while it drops double exponentially with increasing F in the limit of large forces:

$$\lim_{F_R \to \infty} p(F_R) \approx \frac{k_0}{\dot{F}} \exp\left[-\frac{k_0 k_B T}{\dot{F}\Delta x_0} \exp\left(\frac{F_R \Delta x_0}{k_B T}\right)\right]. \tag{12}$$

This leads to the skewness in $p(F_R)$, where the rise preceding the $p(F_R)$ peak is more gradual than the drop after the peak. The theoretical $p(F_R)$ also correctly predicts the characteristic shift in $p(F_R)$ towards larger forces with increasing loading rate $\dot{F}$. This effect can also be intuitively explained by Equation (8): $k(F)$ is independent of $\dot{F}$, but $S(t)$ decays more slowly with increasing $\dot{F}$ when plotted as a function of the rupture force

(Figure 4(B)), causing the rightwards shift in $p(F_R)$ (Figure 4(C)). Note that the slower decay in $S(F_R)$ occurs because a force F_R is reached faster at larger loading rates, giving the bond less time to undergo thermally activated rupture.

It is possible to calculate a semianalytic expression for the mean rupture force $\overline{F_R} = \int_0^\infty F_R p(F_R) dF_R$ corresponding to the $p(F_R)$ in Equation (10):

$$\overline{F_R} = \frac{k_B T}{\Delta x_0} \exp\left[\frac{k_0 k_B T}{\dot{F} \Delta x_0}\right] E_1\left(\frac{k_0 k_B T}{\dot{F} \Delta x_0}\right), \tag{13}$$

where $E_1(x)$ is the exponential integral $\int_x^\infty e^{-t}/t \, dt$ that can be approximated as $e^{-x} \ln(1 + e^{-\gamma}/x)$ with $\gamma \approx 0.577$. Similarly, the location of the peak in $p(F_R)$, known as the most probable force $F_{R,mp}$, may be evaluated analytically by setting the derivative $dp(F_R)/dF_R|_{F_{R,mp}} = 0$:

$$F_{R,mp} = \frac{k_B T}{\Delta x_0} \ln\left(\frac{\dot{F} \Delta x_0}{k_0 k_B T}\right). \tag{14}$$

These results indicate that $\overline{F_R}$ and $F_{R,mp}$ rise near-logarithmically and logarithmically with increasing loading rate (Figure 4(D)), respectively, and that both forces increase with decreasing distance to barrier Δx_0 and decreasing intrinsic rupture rate k_0. The above models, especially Equations (13) and (14), have allowed researchers to extract the energy landscape parameters k_0 and Δx_0 from measurements of rupture forces conducted in the force-ramp mode.[17,18]

3. Second-generation models

The Bell–Zhurkov model correctly predicts many features of force-induced rupture in both the constant-force and constant speed pulling modes, but suffers from several limitations due to its phenomenological nature. In particular, the model lumps all features of the energy landscape into a single parameter, the barrier distance Δx_0, assuming that the external force affects only the energy barrier (lowering it by $F\Delta x_0$). However, as discussed below, the force-perturbed landscape exhibits not only a reduction in the energy barrier but also a reduction in the barrier distance, resulting in a rupture rate that depends on the shape of the energy landscape. The departure from the Bell–Zhurkov rate becomes more severe at modest to large forces, limiting the validity of the Bell–Zhurkov model to small forces and slow pulling rates. These limitations were first recognised by Evans and Ritchie [15], who employed Kramers' theory [19] to capture the effect of force-induced changes in the shape of the landscape on the rupture rates $k(F)$ and the distribution $p(F_R)$ of rupture forces. While this initial effort only led to approximate models, subsequent efforts have led to more sophisticated models. Before describing these models based on Kramers' theory, we provide some essential details of this classic theory, following closely the derivation provided by Hänggi and coworkers [20].

3.1. Kramers' theory of reaction rate at high friction

In 1940, Kramers provided an elegant, closed-form solution for the rate of escape of a Brownian particle over a potential energy barrier. While the original theory treats weak, moderate and high-friction cases, we limit our discussion to the latter regime, which is the most applicable to SMFS experiments.

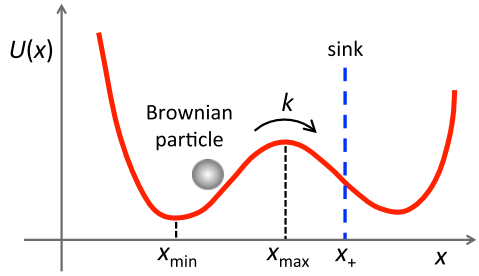

Figure 5. Schematic of the setup used by Kramers to derive the rate of escape k of a Brownian particle trapped within a potential well (see text for details).

The theory considers Brownian motion of a particle along a single coordinate x within a position-dependent potential energy field $U(x)$ exhibiting a minimum at $x = x_{min}$ and a barrier at $x = x_{max}$ (Figure 5). The particle experiences two kinds of forces: a deterministic force $-dU/dx$ arising from the field and a stochastic force $\xi(t)$ arising from external friction. Under conditions of high friction, the particle undergoes stochastic motion and its position $\xi(t)$ can be described by the overdamped Langevin equation [20,21]:

$$\frac{dx}{dt} = \frac{1}{\zeta}\left[-\frac{dU}{dx} + \xi(t)\right], \tag{15}$$

where ζ is the friction constant given by the ratio of the viscous drag force exerted by a stationary fluid on a moving particle to the particle velocity; for a sphere of radius R in a fluid of viscosity η, Stokes law gives $\zeta = 6\pi\eta R$. The fluctuating force $\xi(t)$ is assumed to be a Gaussian-distributed random variable uncorrelated in time with zero mean and variance of $2\zeta k_B T$. In such a scenario, the probability $\rho \equiv \rho(x,t)$ (technically probability density) that the particle is located at position x at time t is governed by the particle-conservation equation

$$\frac{\partial \rho}{\partial t} = -\frac{\partial J}{\partial x}, \tag{16}$$

where $J \equiv J(x,t)$ is the probability flux given by the sum of a diffusive and a 'drift' component:

$$J = -\frac{k_B T}{\zeta}\frac{\partial \rho}{\partial x} - \frac{1}{\zeta}\frac{\partial U}{\partial x}\rho, \tag{17}$$

leading to the well-known Smoluchowski equation.[22] Note that Equations (16) and (17) are analogous to the mass-conservation and molar-flux equations used for describing mass transport in fluids.[23] In the latter case, a molar flux N replaces J, a molar concentration c replaces ρ, a diffusivity D replaces $k_B T/\zeta$ and a convective velocity v replaces the $-(\partial U/\partial x)/\zeta$ term.

To calculate the rate of escape k of a particle from the potential well across the barrier, Kramers assumed that the potential well is sufficiently deep, i.e. $\Delta U \equiv U(x_{max}) - U(x_{min}) >> k_B T$, such that the rate of escape is sufficiently small that it allows the particle to attain a near-equilibrium state inside the well. Next, a special scenario was considered, where the particle is instantly removed when it reaches position $x = x_+ > x_{max}$, after crossing

over the barrier. At the same time, particles are introduced into the well at a rate such that a steady-state flux $J(x)$ and a steady-state probability density $\rho(x)$ is eventually developed. It must then follow from Equation (16) that $J(x)$ is also independent of position; we denote this constant flux by J_0. The rate of escape k gives the conditional probability of escape per unit time given that the particle is present in the well. In contrast, the flux J_0 gives the probability of escape per unit time when the particle has a probability $p_0 = \int_{-\infty}^{x_{\max}} \rho(x)\mathrm{d}x$ of residing within the well, implying that

$$k = J_0/p_0. \tag{18}$$

The flux J_0 can be obtained from Equation (17) by multiplying both sides by the factor $e^{U(x)/k_BT}$ and assimilating the two terms on the right-hand side into a single differential:

$$J_0 = -\frac{k_BT}{\zeta} e^{-U(x)/k_BT} \frac{\partial}{\partial x}\left[\rho(x) e^{U(x)/k_BT}\right]. \tag{19}$$

Integrating the two sides within the limits x_+ and x and recognising that $\rho(x_+) = 0$, we obtain

$$\rho(x) = \frac{\zeta J_0}{k_BT} e^{-U(x)/k_BT} \int_x^{x_+} e^{U(y)/k_BT}\mathrm{d}y. \tag{20}$$

The transition rate k may then be obtained from Equation (18):

$$k = \frac{k_BT}{\zeta}\left[\int_{-\infty}^{x_{\max}} \mathrm{d}x\, e^{-U(x)/k_BT} \int_x^{x_+} \mathrm{d}y\, e^{U(y)/k_BT}\right]^{-1}. \tag{21}$$

The above expression can be further simplified for the case of large barrier heights. Specifically, the outer integral is dominated by the value of $U(x)$ close to the minimum $x_{\min}$ and the inner integral is dominated by values of $U(x)$ close to the maximum $x_{\max}$, whereupon one can invoke the harmonic approximations

$$U(x) \approx U(x_{\min}) + \frac{1}{2}U''(x_{\min})(x - x_{\min})^2, \text{ for small } |x - x_{\min}|, \tag{22}$$

$$U(x) \approx U(x_{\max}) - \frac{1}{2}|U''(x_{\max})|(x - x_{\max})^2, \text{ for small } |x - x_{\max}|. \tag{23}$$

where $U''(x_{\min}) \equiv d^2U/\mathrm{d}x^2|x_{\min}$ and $U''(x_{\max}) \equiv d^2U/\mathrm{d}x^2|x_{\max}$ are the local curvatures of the potential well and barrier regions. These approximations allow the two integrals to be decoupled and analytically evaluated:

$$\int_{-\infty}^{x_{\max}} \mathrm{d}x\, e^{-U(x)/k_BT} \approx e^{-U(x_{\min})/k_BT} \times \sqrt{2\pi k_BT/U''(x_{\min})}, \tag{24}$$

$$\int_x^{x_+} \mathrm{d}y\, e^{U(y)/k_BT} \approx e^{U(x_{\max})/k_BT} \times \sqrt{2\pi k_BT/|U''(x_{\max})|}. \tag{25}$$

Substituting, Equations (24) and (25) into Equation (21) yields the classic result for the barrier-crossing rate:

$$k = \frac{\sqrt{U''(x_{\min})|U''(x_{\max})|}}{2\pi\zeta} e^{-\Delta U/k_BT}. \tag{26}$$

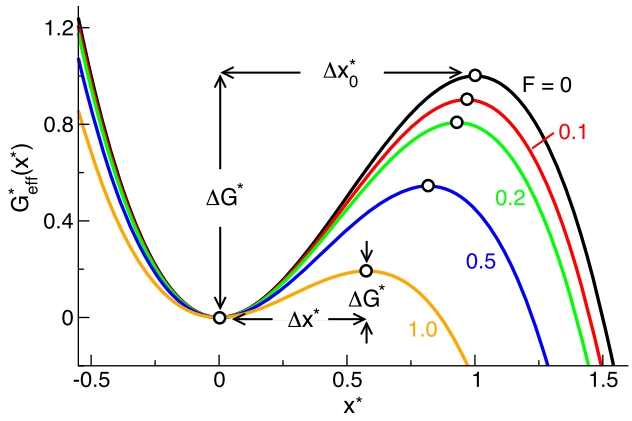

Figure 6. Tilting of an energy landscape by an external force reduces not only the energy barrier ΔG but also the barrier distance Δx. The black curve represents the intrinsic landscape $G(x)$ modeled as a linear-cubic polynomial (Equation (29)) with barrier height ΔG_0 and barrier distance Δx_0. The remaining curves show the tilted landscape $G_{\text{eff}}(x; F) = G(x) - Fx$ for different magnitudes of applied force F as labelled. All curves have been shifted so that their minima are located at $x = 0$ and $G_{\text{eff}} = 0$; the open circles identify the minima and maxima in each curve. All quantities are reported in dimensionless units: $x^* \equiv x/\Delta x_0$, $G^* \equiv G/\Delta G_0$, and $F^* \equiv F\Delta x_0/\Delta G_0$.

Kramers' theory thus suggests that the transition rate decreases with increasing solvent friction and increasing barrier height, both of which are consistent with experimental observations in the high-friction limit. The theory further demonstrates the role of the curvature of the potential energy landscape: sharper curvatures keeping the same barrier height ΔU fixed, which implies a smaller distance between the well and barrier, naturally lead to higher transition rates.

3.2. Application of Kramers' rate to force-tilted model lansdcapes

In a landmark study, Evans and Ritchie [15] demonstrated the utility of Kramers' theory for deriving rupture rates $k(F)$ and rupture forces $p(F_R)$ without resorting to phenomenological models. Several arguments were provided for the relevance of Kramers' theory to SMFS. First, the pulling experiments are typically carried out in a solvent, providing a high-friction environment in which Kramers' high-friction rate (Equation (26)) becomes valid. Second, the molecular systems probed in the experiments are typically stabilised by strong intermolecular interactions, indicating a large energy barrier between the bound and unbound states, another key requirement for the validity of Kramers' theory. Finally, even though a molecular system may intrinsically unfold or unbind through multiple paths within the multi-dimensional conformational space, the application of a stretching force serves to collimate the reaction path along the direction of pulling, providing even stronger basis for the applicability of Kramers theory derived for a single reaction coordinate.

Evans and Ritchie recognised that in the presence of an external force F, the deterministic force $-\partial U/\partial x$ experienced by the particle in Kramers' theory (Equations (15) and (17)) must be replaced by $-\partial U/\partial x + F$, which causes the potential $U(x)$ appearing later in the derivation to be replaced by the effective potential $U(x) - Fx$. They subsequently examined this 'tilting' effect of force F on specific functional forms of the

intrinsic energy landscape $G(x)$; note that the potential energy $U(x)$ used in Kramers' theory has been replaced by the potential of mean force $G(x)$. The resulting effective landscape $G_{\text{eff}}(x; F) = G(x) - Fx$ exhibited not only a reduction in the energy barrier $\Delta G(F)$ with increasing force, as proposed by Bell, but also a reduction in the distance $\Delta x(F)$ to the barrier along and non-trivial changes in the curvature of the potential well and barrier regions. Figure 6 illustrates these effects for a model landscape described by the linear-cubic polynomial discussed below. Note that, contrary to Bell's proposition, the barrier does not disappear at a force F equal to $\Delta G_0/\Delta x_0$. By deriving approximations for $\Delta G(F)$ and the curvatures $G''(x_{\text{min}}; F)$ and $G''(x_{\text{max}}; F)$ and substituting them into Kramers' rate (Equation (26)), Evans and Ritchie obtained approximate scalings for the dependence of $k(F)$ on the applied force F.

Since this work, significant progress has been made on the application of Kramers' theory to other energy landscape models, [16,24–28] examining the properties of the predicted rupture rates and forces,[25,26,29] testing the assumptions of Kramers' theory as applied to pulling experiments,[30,31] studying molecular transitions in multi-dimensional landscapes,[32] and elucidating the effects of the roughness of the energy landscape on transition rates.[33,34]

We restrict our discussion to the seminal work of Dudko, Hummer, and Szabo [25], who examined two different functional forms of the energy landscape to derive analytical expressions for $k(F)$, $p(F_{\text{R}})$, and $\overline{F_{\text{R}}}$ as a function of the parameters k_0, ΔG_0 and Δx_0 of the energy landscape. To combine the results from the two model landscapes into a unified framework, an additional parameter ν that characterises the shape of the energy landscape was proposed. The resulting model provides a powerful means for recovering properties of the underlying energy landscape from rupture rate and force measurements. The two energy landscape models that were examined are the linear-cubic potential (Equation (27)) and the cusp potential (Equation (28)):

$$G(x) = \frac{3}{2}\Delta G_0 \left(x/\Delta x_0\right) - 2\Delta G_0 \left(x/\Delta x_0\right)^3, \tag{27}$$

$$G(x) = \begin{cases} \Delta G_0 \left(x/\Delta x_0\right)^2 & x < \Delta x_0 \\ -\infty & x \geq \Delta x_0 \end{cases}, \tag{28}$$

which were designed to exhibit an energy barrier of ΔG_0 and a barrier distance of Δx_0. Below we demonstrate how $k(F)$ was derived for the linear-cubic potential. We leave the corresponding derivation for the cusp potential as an exercise for the readers.

The intrinsic linear-cubic potential exhibits a minimum at $x_{\text{min}} = -\Delta x_0/2$ with $G(x_{\text{min}}) = -\Delta G_0/2$ and a maximum at $x_{\text{max}} = \Delta x_0/2$ with $G(x_{\text{max}}) = \Delta G_0/2$. The application of force F tilts the energy landscape, yielding the effective landscape

$$G_{\text{eff}}(x; F) = \frac{3}{2}\Delta G_0 \left(x/\Delta x_0\right) - 2\Delta G_0 \left(x/\Delta x_0\right)^3 - Fx, \tag{29}$$

whose minimum and maximum get shifted inwards towards $x = 0$ and $G_{\text{eff}} = 0$, reducing both the barrier distance $\Delta x(F) \equiv x_{\text{max}}(F) - x_{\text{min}}(F)$ and the barrier height $\Delta G(F) \equiv G_{\text{eff}}(x_{\text{max}}(F); F) - G_{\text{eff}}(x_{\text{min}}(F); F)$ (see Figure 6). It can be shown that the locations of the new force-dependent minimum and maximum are given by

$$x_{\text{min}}(F) = -\frac{\alpha \Delta x_0}{2}, \quad x_{\text{max}}(F) = \frac{\alpha \Delta x_0}{2}, \tag{30}$$

where $\alpha \equiv \alpha(F) = \left(1 - 2F\Delta x_0/3\Delta G_0\right)^{1/2}$. The free energy values at the two extrema are:

$$G_{\text{eff}}(x_{\text{min}}) = -\frac{\alpha^3 \Delta G_0}{2}, \quad G_{\text{eff}}(x_{\text{max}}) = \frac{\alpha^3 \Delta G_0}{2}, \tag{31}$$

and the local curvatures at the two points are:

$$G''_{\text{eff}}(x_{\text{min}}) = \frac{6\alpha \Delta G_0}{{\Delta x_0}^2}, \quad G''_{\text{eff}}(x_{\text{max}}) = -\frac{6\alpha \Delta G_0}{{\Delta x_0}^2}. \tag{32}$$

Substituting $\Delta G(F)$, $G''_{\text{eff}}(x_{\text{min}}(F); F)$ and $G''_{\text{eff}}(x_{\text{max}}(F); F)$ into Kramers' rate (Equation (26)) and comparing the resulting expression with the intrinsic rate constant $k_0 \equiv k(0)$ yields

$$k(F) = k_0 \left(1 - \frac{2F\Delta x_0}{3\Delta G_0}\right)^{1/2} \exp\left[\frac{\Delta G_0}{k_{\text{B}}T}\left\{1 - \left(1 - \frac{2F\Delta x_0}{3\Delta G_0}\right)^{3/2}\right\}\right]. \tag{33}$$

The rate $k(F)$ corresponding to the cusp potential can be derived similarly.

Comparing the rates from the linear-cubic and cusp potentials and the Bell–Zhurkov model (Equation (3)), Dudko et al. realised that all three rates could be combined into a unified framework:

$$k(F) = k_0 \left(1 - \frac{\nu F\Delta x_0}{\Delta G_0}\right)^{1/\nu - 1} \exp\left[\frac{\Delta G_0}{k_{\text{B}}T}\left\{1 - \left(1 - \frac{\nu F\Delta x_0}{\Delta G_0}\right)^{1/\nu}\right\}\right], \tag{34}$$

with $\nu = 1/2$, $2/3$ and 1 yielding rates for the cusp, linear-cubic and Bell–Zhurkov models. The results illustrate how the effect of the imposed force is distinct from that of the Bell–Zhurkov model: the force reduces the energy barrier by an amount smaller than $-F\Delta x_0$ prescribed by the phenomenological model and it also reduces the curvatures of the potential well and barrier causing a reduction in the barrier distance, all of which are assumed to be fixed in Bell–Zhurkov model. The first of these effects appears in the exponential term in Equation (33) and the second effect appears in the prefactor. Both effects contribute to a reduction in the rupture rate *relative* to Bell–Zhurkov rate, especially at large forces (Figure 7(A)). Indeed, it can be shown that the rates from both models reduce to the Bell–Zhurkov model at small forces $F << \Delta G_0/\Delta x_0$. It is also noted that the new rate expressions are functions of not only Δx_0 and k_0, but also of ΔG_0, enabling a more complete description of the underlying energy landscape to be recovered by fitting Equation (34) to experimentally measured $k(F)$. The above framework also reveals the role of the shape of the energy landscape in dictating rupture rates. This role is embodied in the parameter ν, which can be fitted to experimental results to yield information about the shape of the energy landscape.

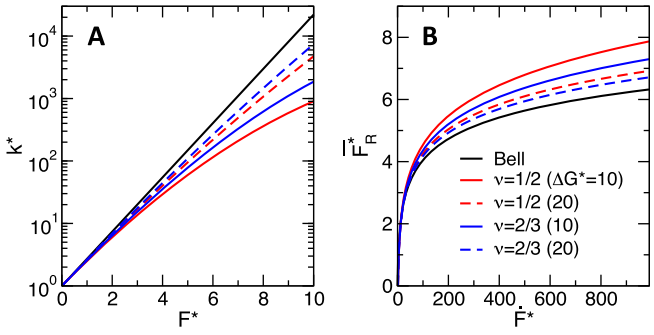

Figure 7. Bell–Zhurkov model overpredicts rupture rates and underpredicts rupture forces, especially at large loads and loading rates. Comparison of Dudko–Hummer–Szabo model using the cusp model potential ($\nu = 1/2$) (red lines) and the linear-cubic model potential ($\nu = 2/3$) (blue lines) for two different landscapes with barrier heights $\Delta G_0^* = 10$ (solid lines) and 20 (dashed lines) against the Bell–Zhurkov model (black lines). (A) Rupture rate k^* versus imposed force F^*, and (B) average rupture forces $\overline{F_R^*}$ versus loading rate $\dot{F}^*$. All quantities are reported in dimensionless units: $\Delta G^* \equiv \Delta G/k_BT$, $k^* \equiv k/k_0$, $F^* \equiv F\Delta x_0/k_BT$, $\overline{F_R^*} \equiv \overline{F_R}\Delta x_0/k_BT$, and $\dot{F}^* \equiv \dot{F}\Delta x_0/k_0k_BT$.

3.3. Rupture forces under linearly-increasing loads

The rates $k(F)$ derived above were subsequently used within the survival-probability formalism (Equation (9)) to obtain the rupture force distribution, which can also be cast in the unified form through the use of the shape parameter ν:

$$p(F_R) = \frac{k(F_R)}{\dot{F}} \exp\left[\frac{k_0 k_B T}{\dot{F}\Delta x_0}\right] \exp\left[-\frac{k(F_R)k_BT}{\dot{F}\Delta x_0}\left\{1-\left(\frac{\nu F_R \Delta x_0}{\Delta G_0}\right)\right\}^{1-1/\nu}\right]. \quad (35)$$

Again, setting $\nu = 1$ results in the $p(F_R)$ derived earlier using the Bell–Zhurkov model (Equation (10)). It was also possible to obtain analytical approximations for the mean $\overline{F_R} = \int_0^\infty F_R p(F_R) dF_R$ and variance $\sigma_{F_R}^2 = \overline{F_R^2} - \overline{F_R}^2$ of the above force distribution:

$$\overline{F_R} \approx \frac{\Delta G_0}{\nu \Delta x_0}\left\{1-\left[\frac{k_BT}{\Delta G_0}\ln\frac{k_0k_BTe^{\Delta G_0/k_BT+\gamma}}{\dot{F}\Delta x_0}\right]^\nu\right\} \quad (36)$$

$$\sigma_{F_R}^2 \approx \frac{1}{6}\left(\frac{\pi k_BT}{\Delta x_0}\right)^2\left[\frac{k_BT}{\Delta G_0}\ln\frac{k_0k_BTe^{\Delta G_0/k_BT+\tilde{\gamma}}}{\dot{F}\Delta x_0}\right]^{2\nu-2}, \quad (37)$$

where $\gamma = 0.577$ and $\tilde{\gamma} = 1.064$. Interestingly, $\gamma = 0$ yields a good approximation for the most probable force $F_{R,mp}$. As with Bell–Zhurkov model, the mean rupture force increases with increasing barrier height ΔG_0 and loading rate $\dot{F}$ and decreasing barrier distance Δx_0 and rate k_0, though the precise dependencies are more complex. Consistent with the results for the rupture rates, the above model predicts higher rupture forces than the Bell–Zhurkov model for the same loading rates (Figure 7(B)).

4. Third-generation models

4.1. Modeling effects of device stiffness

In the models described so far, the pulling device has been assumed to be 'soft', where the device stiffness K is much smaller than the stiffness of the molecular system being studied. This leads to a linear tilting of the energy landscape along the pulling direction via $G_{eff}(x; F) = G(x) - Fx$, and also results in the imposition of a linearly increasing force given by $F(t) = KVt$. However, both of these considerations no longer hold true when the device stiffness is not negligible, as recently demonstrated by Maitra and Arya [35].

To investigate the first consideration, a combined free energy landscape of the molecule and pulling device for the configuration shown in Figure 8 is formulated.[16,24,35] Here, a pulling device with a probe of Hookean stiffness K is directly linked to a molecule (or connected via a rigid linker) whose intrinsic free energy $G(x)$ along the pulling coordinate x exhibits a minimum at $x = 0$. Before pulling commences, the molecule is assumed to be thermally equilibrated in the potential well and the molecular coordinate resides on average at position $x = 0$. At time $t = 0$, the device is moved in the positive-x direction at speed V. At time t, the device has moved a distance Vt, leading to a net deflection of $(Vt - x) \equiv \delta x$ in the probe from its equilibrium position for a molecular coordinate at position x. The combined free energy of the molecule and the device is then given by

$$G_{eff}(x; t) = G(x) + \frac{1}{2}K\left(Vt - x\right)^2. \quad (38)$$

Expanding the second term and ignoring the resulting $\frac{1}{2}KV^2t^2$ term, which only translates the energy landscape upwards without having any effect on the rupture rate, yields:

$$G_{eff}(x; t) = G(x) - KVtx + \frac{1}{2}Kx^2. \quad (39)$$

The second term is the usual force-induced tilting of the energy landscape that *lowers* the energy barrier for rupture. The third term, usually ignored, represents a contribution from the device that, in contrast, *raises* the energy barrier ΔG, as illustrated in Figure 9 using the example of a linear-cubic potential. Physically, this term represents the additional energy required for the molecule to push the pulling device for it to cross over the energy barrier. Another effect of this term is extending the distance Δx to the barrier, as noted from Figure 9.

To investigate the second consideration, we examine the force experienced by the molecule. We assume quasi-static pulling conditions, where V is small enough to allow the molecule and pulling device to thermally equilibrate. In such a scenario, the force $F(t) = K(Vt - x)$ imposed by the deflected probe should roughly balance out the force $K_m x$ developed in the molecule, where K_m is the effective stiffness of the molecule characterised by the curvature $G''(x)|_{x=0}$ of the intrinsic landscape. By equating the two forces, similar to what is done when two springs are placed in series, it can be shown that the molecule experiences a force

$$F(t) = \frac{KVt}{\chi}, \text{ where } \chi \equiv 1 + K/K_m, \quad (40)$$

which is clearly lower than the 'apparent' force $F_1(t) = KVt$ one might estimate purely from the displacement (Vt) of the pulling device. The above springs-in-series formulation further reveals that the device displacement Vt is related to the mean displace-

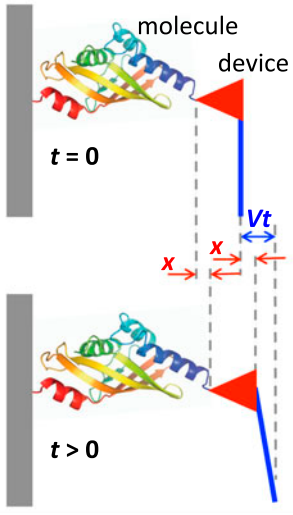

Figure 8. Schematic of a pulling experiment in which the device (AFM cantilever) is directly connected to the molecule. At time $t > 0$, the device has translated by an amount Vt and the concurrent displacement in the molecular coordinate is x.

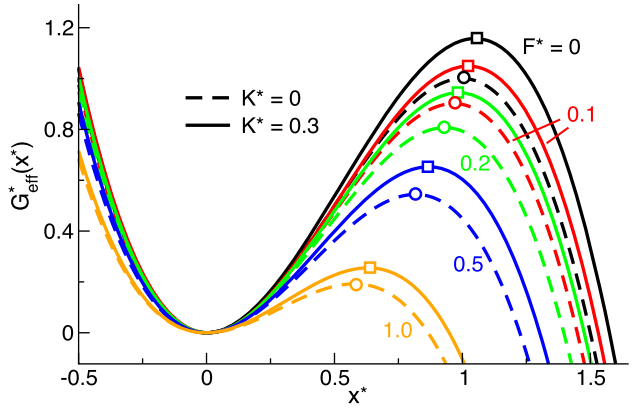

Figure 9. Device stiffness raises the energy barrier and extends the barrier distance from the minimum. Comparison of the intrinsic and force-tilted energy landscape pulled with an infinitely soft pulling device with $K^* \to 0$ (dashed lines, with maxima marked by open circles) and a moderately stiff pulling device with $K^* = 0.3$ (solid lines, with maxima marked by open squares), which is still 20 times softer than the molecule with an effective stiffness of $K_m^* = 6$. Five different force levels in the range $F^* = 0$ to 1 are considered, specified in the figure. All quantities are reported in dimensionless units: $x^* \equiv x/\Delta x_0$, $G^* \equiv G/k_BT$, $F^* = F\Delta x_0/k_BT$, and $K^* \equiv K\Delta {x_0}^2/\Delta G_0$.

ment $\langle \xi(t) \rangle$ and deflection $\langle \delta x(t) \rangle$ of the molecular coordinate and probe at time t (before rupture) via

$$\langle x(t) \rangle = [K/(K + K_m)]Vt = (K/K_m)\,\langle \delta x(t) \rangle\,, \qquad (41)$$

indicating that only for infinitely soft probes ($K << K_m$) do the device displacement and probe deflection become identical. Similarly, only for infinitely stiff probes ($K >> K_m$) does the displacement in molecular coordinate follow that of the device.

The ensuing discussion shows that a stiff pulling device serves to raise the energy barrier and extend the distance to barrier and also causes the molecule to experience a smaller pulling force than that measured from device displacement, all of which inhibit the rupture transition. Considering the characteristic variation in $G(x)$ by the barrier height ΔG_0 and the characteristic variation in x by the barrier distance Δx_0, Equation (39) shows that the effect of device stiffness is negligible only when $K << 2\Delta G_0/\Delta {x_0}^2$, which provides a reasonable criterion for a 'soft' device. This criterion also implies that $K << K_m$, given that the stiffness of the molecule is also on the order of $2\Delta G_0/\Delta {x_0}^2$. Thus, for soft devices, Equation (39) reduces to the usual landscape-tilting effect of the force $G_{eff}(x; t) \approx G(x) - F(t)x$ and Equation (40) reduces to the usual force $F(t) \approx KVt$ used for deriving the earlier models. The parameter χ introduced above thus characterises the extent of departure from the soft-device approximation.

While several studies have examined the effect of device stiffness in modulating the rupture rates and forces through simulations,[36,37] we will focus the remaining discussion on the work of Maitra and Arya [35], who succeeded in obtaining analytical models quantifying these effects in an elegant manner. For this purpose, the authors adopted a shifted version of the linear-cubic potential as the intrinsic energy landscape:

$$G(x) = \frac{3\Delta G_0}{2\Delta x_0}\left(x - \Delta x_0/2\right) - \frac{2\Delta G_0}{{\Delta x_0}^3}\left(x - \Delta x_0/2\right)^3, \qquad (42)$$

so that its minimum is located at $x = 0$. For this model landscape, the parameter χ is given by

$$\chi \equiv \chi(K) = 1 + K\Delta {x_0}^2/6\Delta G_0. \qquad (43)$$

The intrinsic energy landscape (Equation (42)) was next modified using Equation (39) and the time-dependent energy barrier $\Delta G(x; t)$ and time-dependent curvatures $G''(x; t)$ at the minimum and maximum of the modified landscape were determined analytically as a function of time t. Substituting these quantities into Kramers' rate expression (Equation (26)), replacing KVt with $\chi(F)$ (where F is the true force experienced by the molecule) and comparing the resulting rate to the intrinsic rupture rate k_0 yielded the following analytical form for the force-dependent rupture rate:

$$k(F) = k_0\left(\chi^2 - \frac{2F\Delta x_0}{3\Delta G_0}\chi\right)^{1/2} \exp\left[\frac{\Delta G_0}{k_BT}\left\{1 - \left(\chi^2 - \frac{2F\Delta x_0}{3\Delta G_0}\chi\right)^{3/2}\right\}\right]. \qquad (44)$$

Note that the above expression reduces to the result derived earlier for soft devices with $\nu = 2/3$ (Equation (33)) when $\chi \to 1$ ($K \to 0$). The above result plotted in Figure 10(A) for different stiffness values demonstrates that the rupture rate decreases with increasing stiffness (increasing χ) of the pulling device, as illustrated in and as explained earlier in physical terms. Intriguingly, the rupture rates, especially at small forces, do not converge to the rates obtained with soft devices ($K = 0$) even when $K << 6\Delta G_0/\Delta {x_0}^2$. It was found from asymptotic analyses that the true soft-device criterion is $K << 2k_BT/\Delta {x_0}^2$, a much stricter condition than specified above.

One can also derive an analytical form of the rupture force distribution $p(F_R)$ under dynamic loading conditions using the above rupture rate in Equation (9), noting that the true loading rate $\dot{F} \equiv dF/dt$ experienced by the molecule is equal to KV/χ (and not KV):

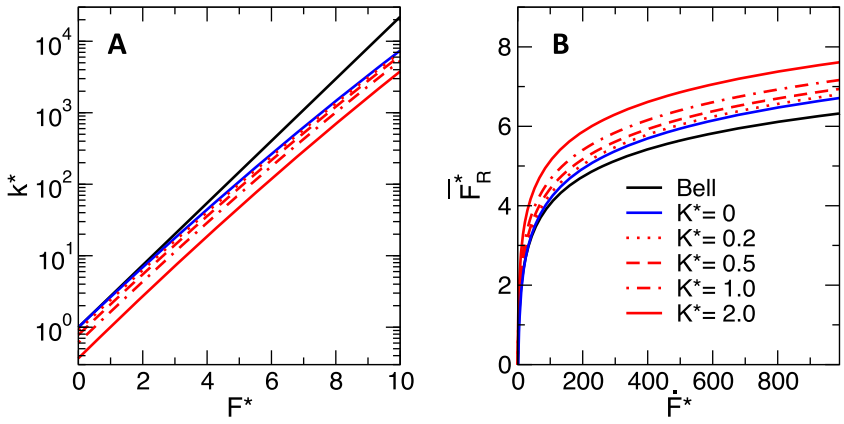

Figure 10. Device stiffness lowers rupture rates and raises rupture forces. Comparison of (A) rupture rates k^* and (B) mean rupture forces predicted from the Maitra-Arya model for pulling devices with stiffness varying in the range $K^* = 0$ to 2; the effective stiffness of the molecule is $K_m^* = 120$. The rupture rates are plotted as a function of imposed force F^* and the mean rupture forces $\overline{F_R^*}$ are plotted as a function of the imposed loading rate $\dot{F}$ for the linear-cubic landscape with an energy barrier of $\Delta G_0^* = 20$. The results for $K^* = 0$ reduce to the Dudko–Hummer–Szabo model with $\nu = 2/3$. Results from Bell–Zhurkov model are shown for reference. All quantities are reported in the same dimensionless units as in Figure 7.

$$p(F_R) = \frac{k(F_R)e^{qX}}{\dot{F}} \exp\left[-\frac{k(F_R)k_BT}{\dot{F}\chi\Delta x_0}\left(\chi^2 - \frac{2F_R\Delta x_0}{3\Delta G_0}\chi\right)^{-1/2}\right], \quad (45)$$

where $q \equiv \exp[(1-\chi^3)\,\Delta G_0/k_BT] \approx \exp[-0.5K\Delta x_0{}^2/k_BT]$ and $X \equiv k_0k_BT/\chi\dot{F}\Delta x_0$. The mean and variance of the rupture force distribution were also derived:

$$\overline{F_R} \approx \frac{3\chi\Delta G_0}{2\Delta x_0}\left[1 - \left\{1 - \frac{k_BT}{\Delta G_0}\frac{e^{qX}E_1(qX)}{\chi^3}\right\}^{2/3}\right], \quad (46)$$

$$\sigma_{F_R}^2 \approx \frac{1}{6}\left(\frac{\pi k_BT}{\Delta x_0}\right)^2 \frac{1}{\chi^4(1+qX)^2}\left[1 - \frac{k_BT}{\Delta G_0}\frac{e^{qX}E_1(qX)}{\chi^3}\right]^{-2/3}, \quad (47)$$

where E_1 is the exponential integral introduced earlier. Again, it can be observed that when $\chi \to 1$ (also causing $q \to 1$), $p(F_R)$, $\overline{F_R}$ and $\sigma_{F_R}^2$ all reduce to the expressions derived under soft-device approximation for $\nu = 2/3$ (Equations (35)–(37)). Inspection of Equations (46) and (47) reveals that an increase in device stiffness K (or χ) leads to increases in both the mean rupture force, as shown in Figure 10(B), and the variance of the rupture force distribution due to the physical reasons mentioned earlier. On the whole, these results (Equations (44) and (46)) imply that experimental data analysed with models derived using soft devices (e.g. Equations (33) and (36)) will overpredict parameters like ΔG_0 and Δx_0 (which cause a reduction in rupture rate and increase in rupture forces) and underpredict parameters like k_0 (which cause the opposite effects). A thorough discussion on the errors involved in neglecting device stiffness can be found in the original study.[35] Also, analogous expressions for $k(F;\chi)$, $p(F_R;\chi)$, $\overline{F_R}(\chi)$ corresponding to the cusp potential are now available from Bullerjahn et al. [28].

4.2. Modelling combined effects of device stiffness and pulling handles

We discuss here the most general case of a pulling device connected to the molecular system via an intervening polymeric 'handle', typically a robust, inert polymer like DNA or poly (ethylene glycol) that prevents non-specific interactions between the device and the molecule. It is well known [38–42] that polymer handles, as a result of their non-linear elasticity, can alter rupture rates and forces in highly non-trivial ways and capturing such effects in an analytical framework is highly desirable. Maitra and Arya [43] showed that the most rigorous approach of treating such a system is to write down the combined free energy of the device, handle, and molecule, as done earlier for the simpler case of the device connected directly to the molecule. In addition to the molecular coordinate x, a second coordinate x_1 specifying the position of the end of the handle attached to the device needs to be introduced (see Figure 11). The combined free energy of the system can now be written as

$$G_{eff}(x, x_1; t) = G(x) + G_d(Vt - x_1; t) + G_h(x_1 - x; t), \quad (48)$$

where $G(x)$ specifies, as usual, the intrinsic free energy of the molecule along the pulling coordinate, $G_d(Vt - x_1; t) = \frac{1}{2}K(Vt - x_1)^2$ specifies the free energy of the pulling device of Hookean stiffness K as a function of probe displacement $Vt - x_1$, and $G_h(\lambda; t)$ specifies the free energy of the handle as a function of its extension $\lambda \equiv x_1 - x$. For a relatively stiff polymeric handle like DNA, this free energy is typically treated using the worm-like chain (WLC) model [44]:

$$G_d(\lambda; t) = \frac{k_BT}{2P}\left[\frac{L}{2\left(1 - \frac{\lambda}{L}\right)} + \frac{\lambda^2}{L} - \frac{\lambda}{2}\right], \quad (49)$$

where P and L are the persistence length and contour length of the polymer chain. For flexible polymers, a freely jointed chain model becomes more appropriate.

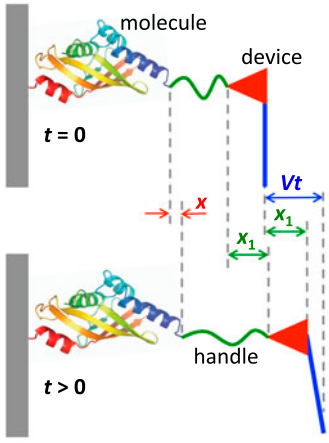

Figure 11. Schematic of a pulling experiment in which the device is connected to the molecule via a molecular handle. At time $t > 0$, the device has translated by an amount Vt. The displacement in the molecular coordinate and the end of the handle are characterised by variables x and x_1, respectively.

To determine rupture rate $k(F)$, one may apply Kramers' theory to the effective free energy landscape $G_{\text{eff}}(x, x_1; t)$ as a function of time t to obtain the rate $k(t)$ and then transform t to the imposed force F using a functional relationship $F(t)$ to obtain $k(F)$. However, this is complicated because the energy landscape is a function of two coordinates. Fortunately, x_1 may be determined as a function of x under conditions of quasistatic pulling. In other words, when the molecule and the polymer relax at a time scale much faster than that associated with pulling, the forces developed within the handle, molecule and device equilibrate rapidly and may be considered for all practical purposes to be equal, thus allowing determination of $x_1(x)$. However, $x_1(x)$ cannot be obtained analytically for a realistic polymer model such as that provided in Equation (48), and a closed-form expression for $k(F)$ could not be derived. Instead, $k(F)$ was obtained numerically by solving for x_1 at progressively increasing times, solving Kramers' equation to obtain $k(t)$, and then transforming t to F via the relation $F(t) = K(Vt - x_1)$. The rupture force distribution $p(F_{\text{R}})$ was then obtained via Equation (9), where the computed loading rate $\mathrm{d}F/\mathrm{d}t$ (instead of KV) was used and the mean rupture force $\overline{F_{\text{R}}}$ was obtained from integrating $p(F_{\text{R}})$ as usual.

The computed $k(F)$ revealed interesting trends with respect to varying K and L values, with $P = 50$ nm fixed to represent double-stranded DNA. It was found that for sufficiently long handles with $L \gtrsim 4\sqrt{P\Delta x_0(\Delta G_0/k_{\text{B}}T)^3}$ or for sufficiently soft devices with $K << 2k_{\text{B}}T/{\Delta x_0}^2$, the rupture rate may be predicted for all forces using the models described earlier. However, when both conditions are not met, the harmonic stiffness K of the device and the anharmonic stiffness K_h of the handle become important and affect the rupture rates and rupture forces in distinct ways. While no analytical model exists for describing the combined effects of the device and handle, the model derived earlier (Equation (44)) with a reparameterised χ parameter was found to provide an excellent approximation for the numerically obtained $k(F)$. In particular, χ, which captured well the stiffness effects arising from the pulling device, was modified to incorporate the combined compliance K' of the handle and the device:

$$\chi(F) = 1 + K'/K_m = 1 + \left[1/K + 1/K_h(F)\right]^{-1}/K_m, \quad (50)$$

where the effective stiffness of the molecule K_{m} and the WLC handle $K_{\text{h}}(F)$ are given by [45]

$$K_{\text{m}} = 6\Delta G_0/\Delta x_0^2, \;\; K_{\text{h}}(F) \approx \frac{3 + 5FP/k_{\text{B}}T + 8(FP/k_{\text{B}}T)^{2.5}}{2FP/k_{\text{B}}T(1 + FP/k_{\text{B}}T)}, \quad (51)$$

With the more complex $\chi(F)$ (Equation (50)) within the rate expression $k(F)$ in Equation (44), analytical expressions for $p(F_{\text{R}})$, or $\overline{F_{\text{R}}}$, could not be obtained. Nonetheless, the parameters k_0, ΔG_0, and Δx_0 may still be inferred from experimentally measured rupture forces by converting $p(F_{\text{R}})$ to $k(F)$ by means of the relationship suggested by Dudko et al. [45]

$$k(F) = \frac{\dot{F}p(F)}{1 - \int_0^F p(F_{\text{R}})\mathrm{d}F_{\text{R}}}, \quad (52)$$

which is essentially the inverse of Equation (9) and can be obtained from Equation (8). Since it is challenging to obtain $\dot{F}$ at the point of rupture due to inherent non-linearity of the F-x relationship, one can estimate this quantity via $\dot{F} = K_{\text{eff}}V$, where $K_{\text{eff}} = (1/K + 1/K_m + 1/K_h)^{-1}$ represents the effective stiffness of the pulling device, molecule, and handle.

As a final note, we emphasise that the force dependence in $k(F)$ discussed so far is assumed to arise from the force-induced tilting effect of the 1D free-energy landscape based on the existence of a single reaction coordinate parallel to the pulling direction. However, one can envision a scenario in which multiple reaction coordinates exist, where a path orthogonal to the pulling coordinate dominates transition rates at equilibrium (zero force) and a path parallel to the pulling coordinate begins to dominate the rate at large forces, due to the biased tilting of the landscape in the pulling direction. In such a case, the experimentally measured $k(F)$ will also include contributions from such a force-dependent switch between two reaction paths. Such an effect is not treated in any of the models discussed so far but is certainly a topic of current interest.[31]

5. Molecular simulations

Molecular simulations are numerical techniques that compute the conformational dynamics of molecules based on their interactions with each other and with external fields. Simulations have played an important role in testing many of the theoretical models presented here, investigating the validity of several of their underlying assumptions, and providing new insights into force-driven molecular transitions. Below, we review two types of simulation approaches that have been used to study such transitions.

5.1. Molecular dynamics

Molecular dynamics (MD) simulations, in their simplest form, involve integration of Newton's equations of motion for each and every atom in the molecular system:

$$\frac{\mathrm{d}\mathbf{r}_i(t)}{\mathrm{d}t} = \mathbf{v}_i(t), \quad (53)$$

$$m_i \frac{\mathrm{d}\mathbf{v}_i(t)}{\mathrm{d}t} = \mathbf{F}_i(t), \tag{54}$$

where m_i is the mass of atom i, and $\mathbf{r}_i$ and $\mathbf{v}_i$ are its position and velocity vectors at time t. $\mathbf{F}_i(t)$ represents the force experienced by the atom, which is calculated as the gradient of the potential energy with respect to atomic position: $\mathbf{F}_i(t) = -\nabla_{\mathbf{r}_i} U$. The total potential energy $U(\mathbf{r}^N)$ for an N-atom system is given by an intramolecular 'force field' accounting for the energies of bond stretching, bond angle bending and dihedral angle rotation, and an intermolecular force field accounting for Coulombic and van der Waals interaction energies. The molecular system is generally confined to a simulation box, of fixed or variable volume V, implementing periodic boundary conditions. The equations of motion in Equations (53) and (54), which simulate the dynamics at constant energy, are usually modified to introduce other constraints, such as constant temperature and/or pressure. The simulated microstates (molecular configurations) $\mathbf{r}^N$ are expected to satisfy the equilibrium probability density distribution of the ensemble (thermodynamic state) being simulated, e.g. Boltzmann distribution $\rho(\mathbf{r}^N) \propto \exp[-U(\mathbf{r}^N)/k_\mathrm{B}T]$ in the canonical (constant-T) ensemble. For details of the force field, integration algorithms, and various other technicalities of MD simulations, we refer readers to several excellent textbooks on this subject.[46–48]

The most evident use of MD simulations has been in elucidating the molecular interactions responsible for the 'apparent' strength of biomolecules or their complexes (resisting their unfolding or dissociation) observed in SMFS experiments. To mimic the force-ramp experiment, the simulations hold one end of the molecule fixed and attach a harmonic spring to the other end that is pulled at constant speed via its free end. Using such a protocol, researchers have examined forced unfolding of a number of protein and protein domains [49,50] and the forced dissociation of a variety of protein complexes,[51,52] with the avidin-biotin complex being one of the first studied systems. Another application has been in investigating the validity of the pulling direction as the natural coordinate for molecular unfolding and dissociation.[31,53,54] MD simulations have also played a key role in elucidating the effects of the stiffness of the pulling device on the measured rupture forces,[37] motivating the development of models accounting for such effects.[35] With the rapid, continuing increase in supercomputing power,[55] MD simulations are expected to play an increasingly important role in the design and interpretation of SMFS experiments.

5.2. Langevin and Brownian dynamics

The MD simulations described above compute the dynamics of *all* atoms in the system, those of the molecule being studied and of the surrounding medium, which may include solvent molecules and ions. Due to limitations on the largest timestep that can be used for integrating the equations of motion (~1 fs), the computational cost associated with studying the dynamics of reasonable-sized molecules beyond 10–100 ns becomes prohibitive. Furthermore, in many cases, one is not interested in the detailed dynamics of the entire molecule being pulled but only of the molecular coordinate describing the transition being investigated.

The time evolution $x(t)$ of this coordinate along the pulling direction, assuming it represents the only relevant reaction coordinate, is described by the Langevin equation, which approximates the effect of reducing the dimensionality of the molecular system from $3N$ to one:

$$\frac{\mathrm{d}x(t)}{\mathrm{d}t} = v(t), \tag{55}$$

$$\frac{\mathrm{d}v(t)}{\mathrm{d}t} = F(t) - \gamma v(t) + \xi(t), \tag{56}$$

where m is an effective mass and $v(t)$ is the velocity of the molecular coordinate. The first term in Equation (56) represents the effective force $F = -\partial G/\partial x$ acting on this coordinate due to the potential of mean force $G(x)$ that arose from the projection of the multi-dimensional energy landscape onto the coordinate x. The second term represents the frictional force (viscous damping) resisting the motion of the molecular coordinate, where γ is a friction constant that is assumed to be independent of x and t.[20] The third term represents a random force arising from the thermal fluctuations in the original degrees of freedom. This random force is generally modelled as a Gaussian white noise (uncorrelated in time) with zero mean:

$$\langle \xi(t) \rangle = 0, \ \left\langle \xi(t)\xi(t') \right\rangle = 2\gamma k_\mathrm{B} T \delta(t - t'). \tag{57}$$

Further simplification of the Langevin equation is possible under conditions of high friction (large γ), a regime relevant to most SMFS experiments, except those conducted at ultrafast force loading. In this scenario, the velocity relaxes much faster than the position, allowing one to set the left-hand side of Equation (56) to zero, leading to the overdamped Langevin equation, also known as the Brownian dynamics (BD) equation:

$$\frac{\mathrm{d}x(t)}{\mathrm{d}t} = \frac{F(t) + \xi(t)}{\gamma}. \tag{58}$$

Thus, the molecular coordinate behaves like a Brownian particle in a viscous solvent, exhibiting a constantly varying 'terminal velocity' according to the instantaneous force it feels from the potential of mean force and from thermal fluctuations.

The primary role of Langevin and BD simulations, especially the latter, in SMFS has been in testing and validating analytical models. For instance, Evans and Ritchie [15] simulated the Brownian motion of a particle confined within a model potential well $G(x)$ and subjected to a linearly increasing force, such that $F(t) = -\partial G/\partial x + \dot{F}t$ in Equation (58). Hundreds of simulations at each loading rate $\dot{F}$ were performed, and in each simulation, the value of the force F_R at which the particle irreversibly crossed the energy barrier was recorded. The distribution $p(F_R)$ in these rupture forces at each $\dot{F}$ reproduced reasonably well those obtained from their analytical model (Equation (10)) using the Bell–Zhurkov expression for the rupture rate. Dudko and coworkers [25] used similar BD simulations to show how well their model for $\overline{F_\mathrm{R}}$ (Equation (35)) and for $k(F)$ (Equation (33)) captured the simulated rupture forces and the rupture rates deduced via Equation (52). Maitra and Arya [35] also used BD simulations, but with the particle connected to a harmonic spring whose free end was pulled at a constant speed, to obtain rupture forces and rates at different spring stiffnesses and

pulling rates, which agreed well with the predictions of their model (Equations (44) and (46)).

Such simulations have also provided many basic insights into force-driven transitions, leading to better interpretation of experiments and more accurate analytical models. For example, BD simulations were key to delineating the non-trivial effects of the pulling device and the molecular handles on the measured rupture rates and forces.[35,43] They have also been used to investigate the degree to which the external force collimates (promotes) molecular trajectories through a transition path collinear with the pulling direction.[31] BD simulations have also helped ascertain the range of validity of the different theoretical models developed over the years.[25,43] Finally, such simulations have revealed novel features in the force-extension behaviour, helped test estimation methods for recovering properties of the energy landscape and elucidated non-equilibrium effects arising from rapid force loading.[28,56,57] To conclude, Langevin and BD simulations, due to their computational tractability and their use of well-defined energy landscapes of any given dimension, will continue to provide important insights into molecular transitions, allowing researchers to validate increasingly sophisticated models and to devise new, more powerful SMFS techniques.

6. Conclusions

This review discusses the theoretical basis for some of the key statistical–mechanical models used for recovering features of the underlying energy landscape governing molecular transitions from single-molecule pulling experiments. Depending on the pulling protocol, these experiments measure either rupture rates as a function of constant applied forces or rupture forces as a function of constant loading rates. We focused on a class of analytical models developed over the years for fitting such measurements of rupture rates and forces and recovering important parameters of the energy landscape, namely, the height ΔG_0 and location Δx_0 of the activation barrier and the rate constant k_0 of the transition. We began by discussing the first-generation models based on the force-rate phenomenological relationship of Bell and Zhurkov. Despite their simplicity, these models have provided excellent approximations for rupture rates and forces as a function of landscape parameters at small forces and loading rates. We next discussed second-generation models, pioneered by Evans and Ritchie, that avoid altogether the use of phenomenological models. Instead, these models apply the theoretical foundation of reaction rates at high friction laid by Kramers to obtain rupture rates and forces for functional forms of the energy landscape. These models go beyond the first-generation models in terms of their wider range of applicability and their ability to recover features of the energy landscape not possible to obtain the earlier models. Lastly, we discussed third-generation models that have extended these models to account for stiffness effects arising from the pulling device and from the polymer handles that connect the molecular system to the device. These models illustrate how the rupture rates and forces get modulated by stiffness effects and how to correct for these effects to recover accurate estimates of the intrinsic parameters of the energy landscape. We concluded by discussing various molecular simulation approaches – molecular dynamics, Langevin dynamics and Brownian dynamics – that have provided and continue to provide new insights into force-driven molecular transitions for better interpretation of the experiments, for developing improved models to analyse force measurements and for devising more informative experimental approaches.

Acknowledgements

The author thanks Dr. Dario Meluzzi for proofreading this article.

Disclosure statement

No potential conflict of interest was reported by the author.

References

[1] Wales D. Energy landscapes: Applications to clusters, biomolecules and glasses. Cambridge: Cambridge University Press; 2003.
[2] Bolhuis PG, Chandler D, Dellago C, et al. Transition path sampling: Throwing ropes over rough mountain passes, in the dark. Ann Rev Phys Chem. 2002;53:291–318.
[3] Roux B. The calculation of the potential of mean force using computer simulations. Comput Phys Commun. 1995;91:275–282.
[4] Woodside MT, Block SM. Reconstructing folding energy landscapes by single-molecule force spectroscopy. Ann Rev Biophys. 2014;43:19–39.
[5] Neuman KC, Nagy A. Single-molecule force spectroscopy: optical tweezers, magnetic tweezers and atomic force microscopy. Nat Methods. 2008;5:491–505.
[6] Hummer G, Szabo A. Free energy reconstruction from nonequilibrium single-molecule pulling experiments. Proc Natl Acad Sci. 2001;98:3658–3661.
[7] Collin D, Ritort F, Jarzynski C, et al. Verification of the crooks fluctuation theorem and recovery of RNA folding free energies. Nature. 2005;437:231–234.
[8] Jarzynski C. Nonequilibrium equality for free energy differences. Phys Rev Lett. 1997;78:2690–2693.
[9] Crooks GE. Entropy production fluctuation theorem and the nonequilibrium work relation for free energy differences. Phys Rev E. 1999;60:2721–2726.
[10] Bell GI. Models for the specific adhesion of cells to cells. Science. 1978;200:618–627.
[11] Zhurkov SN. Kinetic concept of the strength of solids. Int J Fract Mech. 1965;1:311–323.
[12] Schlierf M, Li H, Fernandez JM. The unfolding kinetics of ubiquitin captured with single-molecule force-clamp techniques. Proc Natl Acad Sci. 2004;101:7299–7304.
[13] Marshall BT, Long M, Piper JW, et al. Direct observation of catch bonds involving cell-adhesion molecules. Nature. 2003;423:190–193.
[14] Evans E, Berk D, Leung A. Detachment of agglutinin-bonded red blood cells. I. Forces to rupture molecular-point attachments. Biophys J. 1991;59:838–848.
[15] Evans E, Ritchie K. Dynamic strength of molecular adhesion bonds. Biophys J. 1997;72:1541–1555.
[16] Hummer G, Szabo A. Kinetics from nonequilibrium single-molecule pulling experiments. Biophys J. 2003;85:5–15.
[17] Gergely C, Voegel JC, Schaaf P, et al. Unbinding process of adsorbed proteins under external stress studied by atomic force microscopy spectroscopy. Proc Natl Acad Sci. 2000;97:10802–10807.
[18] Dietz H, Rief M. Exploring the energy landscape of GFP by single-molecule mechanical experiments. Proc Natl Acad Sci. 2004;101:16192–16197.
[19] Kramers HA. Brownian motion in a field of force and the diffusion model of chemical reactions. Physica. 1940;7:284–304.
[20] Hänggi P, Talkner P, Borkovec M. Reaction-rate theory: fifty years after Kramers. Rev Mod Phys. 1990;62:251–341.
[21] McQuarrie DA. Statistical mechanics. Sausalito (CA): University Science Books; 2000.

[22] Smoluchowski M. Brownian molecular movement under the action of external forces and its connection with the generalized diffusion equation. Ann Phys (Leipzig). 1915;48:1103–1112.
[23] Welty JR, Wicks CE, Rorrer G, et al. Fundamentals of momentum, heat, and mass transfer. Hoboken (NJ): John Wiley & Sons; 2009.
[24] Dudko O, Filippov A, Klafter J, et al. Beyond the conventional description of dynamic force spectroscopy of adhesion bonds. Proc Natl Acad Sci. 2003;100:11378–11381.
[25] Dudko OK, Hummer G, Szabo A. Intrinsic rates and activation free energies from single-molecule pulling experiments. Phys Rev Lett. 2006;96:108101.
[26] Freund L. Characterizing the resistance generated by a molecular bond as it is forcibly separated. Proc Natl Acad Sci. 2009;106:8818–8823.
[27] Li D, Ji B. Predicted rupture force of a single molecular bond becomes rate independent at ultralow loading rates. Phys Rev Lett. 2014;112:078302.
[28] Bullerjahn JT, Sturm S, Kroy K. Theory of rapid force spectroscopy. Nat Commun. 2014;5:4463.
[29] Friddle RW. Unified model of dynamic forced barrier crossing in single molecules. Phys Rev Lett. 2008;100:138302.
[30] Li PC, Makarov DE. Simulation of the mechanical unfolding of ubiquitin: Probing different unfolding 19 December 14, 2015 Molecular Simulation Manuscript reaction coordinates by changing the pulling geometry. J Chem Phys. 2004;121:4826–4832.
[31] Best RB, Paci E, Hummer G, et al. Pulling direction as a reaction coordinate for the mechanical unfolding of single molecules. J Phys Chem B. 2008;112:5968–5976.
[32] Suzuki Y, Dudko OK. Single-molecule rupture dynamics on multidimensional landscapes. Phys Rev Lett. 2010;104:048101.
[33] Zwanzig R. Diffusion a rough potential. Proc Natl Acad Sci. 1988;85:2029–2030.
[34] Hyeon C, Thirumalai D. Can energy landscape roughness of proteins and RNA be measured by using mechanical unfolding experiments? Proc Natl Acad Sci. 2003;100:10249–10253.
[35] Maitra A, Arya G. Model accounting for the effects of pulling-device Stiffness in the analyses of singlemolecule force measurements. Phys Rev Lett. 2010;104:108301.
[36] Evstigneev M, Reimann P. Refined force-velocity relation in atomic friction experiments. Phys Rev B. 2006;73:113401.
[37] Walton EB, Lee S, Van Vliet KJ. Extending Bell's model: how force transducer stiffness alters measured unbinding forces and kinetics of molecular complexes. Biophys J. 2008;94:2621–2630.
[38] Friedsam C, Wehle AK, Kühner F, , et al. Dynamic single-molecule force spectroscopy: bond rupture analysis with variable spacer length. J Phys Condens Matter. 2003;15:S1709–S1723.
[39] Ratto TV, Langry KC, Rudd RE, et al. Force spectroscopy of the double-tethered concanavalin-A mannose bond. Biophys J. 2004;86:2430–2437.
[40] Hyeon C, Thirumalai D. Forced-unfolding and force-quench refolding of RNA hairpins. Biophys J. 2006;90:3410–3427.
[41] Evans E, Ritchie K. Strength of a weak bond connecting flexible polymer chains. Biophys J. 1999;76:2439–2447.
[42] Ray C, Brown JR, Akhremitchev BB. Correction of systematic errors in single-molecule force spectroscopy with polymeric tethers by atomic force microscopy. J Phys Chem B. 2007;111:1963–1974.
[43] Maitra A, Arya G. Influence of pulling handles and device stiffness in single-molecule force spectroscopy. Phys Chem Chem Phys. 2011;13:1836–1842.
[44] Marko JF, Siggia ED. Stretching DNA. Macromolecules. 1995;28:8759–8770.
[45] Dudko OK, Hummer G, Szabo A. Theory, analysis, and interpretation of single-molecule force spectroscopy experiments. Proc Natl Acad Sci. 2008;105:15755–15760.
[46] Allen MP, Tildesley DJ. Computer simulation of liquids. Oxford: Oxford University Press; 1989.
[47] Frenkel D, Smit B. Understanding molecular simulation: from algorithms to applications. Vol. 1. San Diego (CA): Academic press; 2001.
[48] Leach AR. Molecular modelling: principles and applications. Harlow: Pearson Education; 2001.
[49] Lu H, Isralewitz B, Krammer A, et al. Unfolding of titin immunoglobulin domains by steered molecular dynamics simulation. Biophys J. 1998;75:662–671.
[50] Gao M, Craig D, Lequin O, et al. Structure and functional significance of mechanically unfolded fibronectin type III1 intermediates. Proc Natl Acad Sci. 2003;100:14784–14789.
[51] Izrailev S, Stepaniants S, Balsera M, et al. Molecular dynamics study of unbinding of the avidin-biotin complex. Biophys J. 1997;72:1568–1581.
[52] Grubmüller H, Heymann B, Tavan P. Ligand binding: molecular mechanics calculation of the streptavidin-biotin rupture force. 1996;271:997–999.
[53] Schlierf M, Rief M, Paci E. Complex unfolding kinetics of single-domain proteins in the presence of force. Biophys J. 2010;99:1620–1627.
[54] Sun L, Noel JK, Sulkowska JI, et al. Connecting thermal and mechanical protein (un) folding landscapes. Biophys J. 2014;107:2941–2952.
[55] Lindor-Larsen K, Piana S, Dror RO, et al. How fast-folding proteins fold. Science. 2011;334:517–520.
[56] Paturej J, Dubbeldam JL, Rostiashvili VG, et al. Force spectroscopy of polymer desorption: Theory and molecular dynamics simulations. Soft Matter. 2014;10:2785–2799.
[57] Chang JC, Fok PW, Chou T. Bayesian uncertainty quantification for bond energies and mobilities using path integral analysis. Biophys J. 2015;109:966–974.